RSC Advances

ROYAL SOCIETY OF CHEMISTRY

www.rsc.org/advances

Facile sonochemical synthesis of near spherical barium zirconate titanate ($BaZr_{1-y}Ti_yO_3$;BZT); perovskite stability and formation mechanism

Supamas Wirunchit [a,c], Thitirat Charoonsuk [a,c] and Naratip Vittayakorn [a,b,c*],

[a] *Electroceramics Research Laboratory, College of Nanotechnology, King Mongkut's Institute of Technology Ladkrabang, Bangkok 10520, Thailand*

[b] *Department of Chemistry, Faculty of Science, King Mongkut's Institute of Technology Ladkrabang, Bangkok 10520, Thailand*

[c] *Advanced Materials Research Unit, Faculty of Science, King Mongkut's Institute of Technology Ladkrabang, Bangkok 10520, Thailand*

**Corresponding author's email: naratipcmu@yahoo.com*

Abstract- The multicationic oxides of perovskite Ba(Zr,Ti)O_3 were synthesized successfully by the sonochemical method without a calcination step. Detailed exploration considering the role of sodium hydroxide (NaOH) concentration, synthesis atmosphere, ultrasonic reaction time and precursor concentration on the perovskite phase formation and particle size was presented. It was found that nanocrystals were formed directly before being oriented and aggregated into large particles in aqueous solution under ultrasonic irradiation. The nucleation in the sonocrystallization process was accelerated by the implosive collapse of bubbles, while the crystal growth process was inhibited or delayed by shock waves and turbulent flow created by ultrasonic radiation. A pure complex perovskite phase of spherical shape was formed completely in a short irradiation time without the calcination process. Sonochemical irradiation could accelerate spherical shape formation of the particles significantly. These results provide new insights into the development and design of better nanomaterial synthesis methods.

Keywords: sonochemical, monodispersed and Barium zirconate titanate

1. Introduction

Barium zirconate titanate ($BaZr_yTi_{1-y}O_3$) and/or $BaZr_yTi_{1-y}O_3$ – based ceramics have become among the most researched lead free piezoelectric materials, due to their excellent piezoelectric properties [1-4]. The conventional solid state method is a traditional way of preparing $BaZr_yTi_{1-y}O_3$ ceramics. However, this fabrication method has several drawbacks such as a long processing time[5, 6], multiple calcinations[7, 8], low purity[9, 10], submicrometer size crystals[5, 6, 11] and a frequent need for grinding steps [10], and this technique is not suitable for obtaining narrow particle size distribution [5, 7, 11]. J. Bera et al. [5] investigated the formation of $BaZr_yTi_{1-y}O_3$ solid solution by using solid state reaction between $BaCO_3$, ZrO_2 and TiO_2. They reported that at a temperature of lower than 1,300°C, raw materials did not form $BaZr_yTi_{1-y}O_3$ solid solution directly because it had a higher formation of energy (133 kcal/mol) than $BaTiO_3$ (34.3 kcal/mol) and $BaZrO_3$ (48.4 kcal/mol). The formation mechanism can be explained by multistep reactions as follows: at the initial stage, $BaTiO_3$ and $BaZrO_3$ are formed separately at a temperature ranging from 700 to 800 °C. Subsequently, the $BaTiO_3$ diffuses into the $BaZrO_3$ to form a single perovskite phase of $BaZr_yTi_{1-y}O_3$ at a temperature as high as 1,600°C. In order to obtain perovskite $BaZr_yTi_{1-y}O_3$ nanoparticles with high quality, many new wet-chemical synthesizing methods have been developed to replace conventional solid state reaction, including the combustion method [12], sol–gel method [13, 14], direct synthesis from solution (DSS) [15], and aqueous co-precipitation method [16]. Nanosized $BaZr_yTi_{1-y}O_3$ particles are synthesized by wet-chemical methods, which make the $BaZr_yTi_{1-y}O_3$ system very attractive for developing new electronic nanodevices [17, 18]. P. Julphunthong *et al* [12] synthesized barium zirconate titanate (BZT) powder via the combustion technique by using Urea $(NH_2)_2CO$ as a fuel to reduce the reaction temperature. Unfortunately, the powder needed to be calcined at 1,000°C for 5 h after the combustion process in order to obtain a pure perovskite structure. Generally, submicron sizes with irregular morphology of the powder are observed always after the calcination process [11, 19]. It is very difficult to obtain nanoparticles of uniform size under the calcination process[11, 19]., which would therefore be an undesirable step during the fabrication process of nanopowder. M. Veitu *et al* [14] reported the synthesis of homogeneous $BaZr_{0.5}Ti_{0.5}O_3$ nanopowders that derived from a alkoxide sol–gel route. The hetero-trimetallic Ba-Ti-Zr framework was synthesized from $[TiZr(OPr^i)_8.Pr^iOH]_2$ and $[Ba(O\ Pr^i{}_2)]$ and used as a precursor. The processing was performed under CO_2-free argon (Ar) or nitrogen atmosphere. The most advantageous characteristics of this method are the high purity and outstanding control of the composition of resulting powders. Nevertheless, the hydrolyzed dried gel needs to be calcined at temperatures above 400°C in order to crystallize $BaZr_yTi_{1-y}O_3$. J. Q. Qi *et al.* [15] developed a new method called direct synthesis from solution (DSS) to prepare $BaZr_yTi_{1-y}O_3$ nanoscaled powders near room temperature under ambient pressure. By dissolving barium hydroxide into warm water as a base solution, nanocrystalline $BaZr_yTi_{1-y}O_3$ powders can be obtained by mixing isopropanal solution of zirconium isopropoxide–isopropanol and tetrabutyl titanate with hot base solution. When doing this, the particle size of the nanoparticles fell within the range of 25 to 120 nm. Recently, single phase nanocrystalline powder of $BaZr_yTi_{1-y}O_3$ was obtained successfully by the aqueous co-precipitation method at a temperature $< 100^oC$ [16]. The process was as follows: a mixed chloride solution of Ba, Ti and Zr ions was dripped slowly into a heated strong base solution (pH>12.0). The nanocrystalline $BaZr_yTi_{1-y}O_3$ favored forming a strongly based concentration at a temperature of about 80^oC. The as-prepared powders showed an average particle size of 30 nm. The precipitant concentration and synthesis temperature play an important role as a parameter for increasing product purity [16]. However, the particles have various shapes such as spherical, acicular, elliptical, and cubic with truncated edges [16]. The particle size and shape are not controlled by this method. The different morphologic shape and wide range of particle size distribution have been the key problem to create the abnormal grain growth in the sintering process[11].

In order to eliminate abnormal grain growth during the sintering process, $BaZr_yTi_{1-y}O_3$ nanoparticles are expected to have spherical morphology with a narrow particle size distribution[11]. Among the wet-chemical methods developed so far[14-16, 20, 21], sonochemical synthesis at ambient temperature seems to be a new technique that fulfills the requirements for synthesizing extremely fine particles with spherical morphology and a narrow size distribution [22, 23]. The sonochemical method uses an acoustic cavitation phenomenon from ultrasonic irradiation to generate or accelerate the chemical reaction. Acoustic cavitation is the formation, growth, and implosive collapse of bubbles in a liquid, which generates a localized hot spot, with a temperature of approximately 5,000 K, pressure of 20 MPa, and heating and cooling rates that exceed 10^{10} K/s [22, 24]. These transient, localized hot spots can drive many chemical reactions, such as decomposition, dissolution, oxidation, reduction, and promotion of polymerization[22, 24]. By using these transient extreme conditions, various kinds of organic, inorganic and novel materials, with unusual properties such as metals [25, 26] , precious metals [27, 28], simple metal oxides [29-35], nitrides [29], carbides [36], sulfides [29, 37] and core/shell nanocomposites [37, 38] were synthesized successfully. Up until now, few studies on the sonochemical synthesis of multicationic oxides based on a complex perovskite structure $[A(B' B'')O_3]$ have been reported, and to the best of the authors' knowledge, there is no previous report on the direct sonochemical synthesis of ($BaZr_yTi_{1-y}O_3$); y =0.0-0.6 powders.

This study used high-intensity ultrasound irradiation to synthesize nanosized complex ternary metal oxide ($BaZr_yTi_{1-y}O_3$); y = 0.0–0.6. Various key synthesis parameters such as synthesis atmosphere, concentration of precipitating agent, concentration of the starting solution, sonication time and Zr/Ti molar ratio were investigated carefully in order to understand their effect on the perovskite phase formation and morphology of the powders. The procedure of the sonochemical formation of nanosized BZT powders also was examined.

2. Experimental procedure

2.1 Solution preparation

In this study, all the reagents used in experiments were of analytical purity and used without further purification. The barium chloride dihydrate ($BaCl_2·2H_2O$, 99.8% Merck), zirconium oxychloride octahydrate ($ZrOCl_2·8H_2O$, 99.5% Advance material) and titanium tetrachloride ($TiCl_4$, 99.9% Wako) were used as the starting materials. Sodium hydroxide (Fisher Scientific 97.7%) was used as the precipitating agent. In order to obtain the stock of Ti–solution, $TiCl_4$ was dripped very slowly into deionized water at a temperature lower than 5°C and stirred vigorously until the solution was clear. Then, the separate stoichiometric amounts of $BaCl_2·2H_2O$ and $ZrOCl_2·8H_2O$ were dissolved typically in de-ionized water in order to obtain the barium (Ba^{2+}) and zirconium (Zr^{4+}) solution, respectively. These stocks of starting solution were prepared freshly for each set of experiments.

2.2 Synthesis of $Ba(Zr_yTi_{1-y})O_3$ powders

The barium zirconate titanate ($Ba(Zr_yTi_{1-y})O_3$; BZT) powder products, with the composition (y) = 0.00, 0.05, 0.20, 0.04 and 0.60, were synthesized by the sonochemical method without the calcination process, which was in accordance with the reaction (1):

$$BaCl_2·2H_2O_{(aq)} + (1\text{-}y)TiCl_{4(aq)} + yZrOCl_2·8H_2O_{(aq)} + (6\text{-}2y)NaOH_{(aq)}$$

$$\rightarrow Ba(Zr_yTi_{1-y})O_{3(s)} + (6\text{-}2y)NaCl_{(aq)} + (13\text{-}y)H_2O_{(aq)} \qquad (1)$$

Firstly, the appropriate proportions of titanium and zirconium (withdrawn from the stock solution using a pipette) were mixed together to form a solution to which the barium solution was then added, with continuous stirring in order to obtain a homogeneous mixed solution. The concentrations of barium and titanium solution were varied from 0.01 mol·L^{-1} to 1.5 mol·L^{-1} in order to study the effect of Ba and Ti ion concentration on the perovskite phase formation. The Ba and Ti ion ratio in the mixed solution was targeted constantly at 1:1. After that, sonication equipment was set up for the sonochemical process. Regarding the synthesis system, the effect of synthesis atmosphere on the phase formation was studied. The powder synthesized in open air was compared with that in a closed system with Ar gas. After setting up the equipment, the sodium hydroxide (NaOH) solution was loaded into a sonication vessel for use as the precipitating agent. The concentration of NaOH solution was varied from 5 to 20 mol.L^{-1} in order to study its effect. Then, the mixed starting solution was added into the sonication vessel, which contained the NaOH solution, drop by drop at a rate of about 25 ml/min. Therefore, a high pH value reached 14 during the process. In order to obtain nanoparticles of better quality, pulse ultrasonication (Sonics VCX-750, 20 kHz, 750 W) was conducted in the 2 s mode; and a pause in 1 s mode was performed in the experiments that followed. It has been reported that synthesized powder in pulse ultrasonic mode gives a narrower particle size distribution than that in continuous ultrasonic mode [39]. This may be related to the uneven distribution of ultrasonic energy in the ultrasonic vessel [39]. During the process of adding mixed solution, white precipitation was formed instantaneously. After the irradiation time was over, the sonication vessel that contained the precipitate was cooled to room temperature by immersing in tap water. Then, the recovered precipitate was filtered out by centrifugal filtration, and washed with de-ionized water until the pH value reduced to 7. The supernatant was checked with 0.1 mol.L^{-1} of $AgNO_3$ solution until no white sediment remained, which confirmed that the chloride ion was not retained. Finally, the washed precipitates were dried at 80^{o}C in an oven overnight in order to obtain the powder products.

2.3 Characterization

The perovskite phase formation, structure and crystallite size of the products were carried out by X-ray powder diffraction using an X-ray diffractometer (Philips PW3040, The Netherlands) with Cu Kα radiation (λ=0.15406 nm). The acceleration voltage was 35 kV with a 150 mA current flux. X-ray diffraction (XRD) was taken of the powders attached to a glass slide, and data were collected in the 2θ range from 20° to 60°, with a scanning rate of 4°/min and sample interval of 0.02°. Crystallite size and microstrain were calculated by the X-ray line broadening method using Scherrer [40] and Hall–Williamson methods [41]. The Scherrer equation relies on utilizing the following equation:

$$D = K\lambda/\beta\cos\theta, \qquad (2)$$

where λ is the CuK_α radiation of wavelength (1.5406Å), β is the full width at haft-maximum (FWHM) in radian and θ is the scattering angle. Also, K is the shape factor (a constant equal to 0.94) and *D* is the crystallite size normalized to the reflecting planes. The Hall-Williamson method provides a technique for finding an average size of coherently diffracting domains and microstrain. Strain-induced peak broadening arises due to imperfect crystal and distortion, which is calculated by using the following formula:

$$\varepsilon = \frac{\beta_{h\,k\,l}}{4tan\theta} \qquad (3)$$

To estimate microstrain from the XRD pattern, Hall and Williamson proposed a formula as follows:

$$\beta_{h\,k\,l}\cos\theta = \frac{\kappa\lambda}{D} + 4\varepsilon sin\theta \qquad (4)$$

where ε is the elastic strain. When $\beta_{h\,k\,l}\cos\theta$ is plotted versus different diffraction planes, a linear fit is expected. Lattice strains were obtained from the slope of this line. Raman spectra were recorded in the 100–1,000 cm^{-1} wave number ranges in order to support the crystal structure identification of synthesized powders with a Thermo Scientific DXR Raman microscope (532-nm excitation of the laser). The vibration mode of the bond in molecules was obtained from Fourier transform infrared (FT-IR spectrum Gx, Perkin Elmer, America) spectra. The morphology and particle size of the resulting as-prepared products were characterized initially by using a scanning electron microscope (SEM, Hitachi 54700), equipped with energy-dispersive X-ray spectroscopy (EDX) capabilities. These samples were then coated conductively with gold by sputtering for 15 s in order to minimize charging effects under SEM imaging conditions. Regarding the study of phase transition, a differential scanning calorimeter (DSC 2920, TA Instrument) was used, and DSC curves were recorded in a temperature range from 30°C to 200°C with a scanning rate of 10°C/min.

3. Results and Discussion

3.1 The effect of NaOH concentration on the perovskite phase formation

Changing the synthetic parameters greatly affected the perovskite phase formation. This study exposed the concentration of NaOH that had a notable effect on the perovskite phase formation. Figure 1 shows the XRD patterns of $BaZr_yTi_{1-y}O_3$; $y = 0.0$ powders that evolved after sonication for 60 min in different NaOH concentrations in the open air system. As shown in Figure 1, only X-ray peaks of whiterite-$BaCO_3$ and $Ba(OH)_2(H_2O)_3$ are present in powder synthesized with 5 mol L^{-1} NaOH. These kinds of unwanted phase correspond well with the literature [21]. No perovskite structure was characteristic of diffraction peaks, thus indicating no reaction had yet been triggered for synthesis with 5 mol L^{-1} of NaOH concentration. Interestingly, the XRD pattern presented no evidence of a Ti-precursor phase, indicating that an amorphous phase might be formed [42]. When the perovskite phase started to form with increasing NaOH concentration, the $BaCO_3$ and $Ba(OH)_2(H_2O)_3$ phase decreased dramatically. Diffraction peaks of the perovskite phase are indexed with the $BaTiO_3$ cubic structure in the *Pm*3*m* space group from JCPDS card No. 31-0174. Intensity of the perovskite pattern increased significantly with increasing NaOH concentration. The increase in perovskite phase at high hydroxide concentration might be due to increasing formation of the complex polymeric chain network of bimetallic Ba-Ti hydroxides [43]. Nevertheless, in the open air system, a peak of $BaCO_3$ with low intensity was still present in products synthesized in 20 mol L^{-1} of NaOH concentration. The problem of forming $BaCO_3$ at a high NaOH concentration should be attributed to use of the open air synthesis system, in which the Ba-hydroxide in the solution can react easily with CO_2 in air or carbonate species in the solution.

3.2 Effect of synthesis atmosphere on the perovskite phase formation

In order to study the influence of synthesis atmosphere on the perovskite phase formation, the powder was synthesized in open-air and Ar atmosphere. Figure 2 shows XRD patterns of $BaZr_yTi_{1-y}O_3$; $y = 0.0$ powders that evolved after sonication for 5 to 60 min in 20 mol.L^{-1} of NaOH concentrations in the (a) open air system and (b) closed system with Ar gas. The XRD pattern in the open-air system showed a mixed phase of perovskite, $BaCO_3$ and $Ba(OH)_2(H_2O)_3$ phases. The $BaCO_3$ and $Ba(OH)_2(H_2O)_3$ phase remained in the pattern with increasing sonication time, indicating that the formation of $BaCO_3$ and $Ba(OH)_2(H_2O)_3$ phase are not related directly with the sonication irradiation time. Regarding powder synthesized in Ar atmosphere, the $BaCO_3$ phase disappeared after only five minutes sonication time. The relatively small XRD pattern agreed well with the perovskite structure. However, intensity of the perovskite phase was quite low, indicating that the product has low crystallinity. The crystallinity of the product was improved significantly by increasing the sonication period, and a sharp XRD pattern was observed clearly at 60 min sonication time. The observations clearly show that the $BaZr_yTi_{1-y}O_3$; $y = 0.0$ phase formation was completed during the sonochemical process itself, without the need of further calcination or a heating process. The

XRD pattern indicated that the synthesized powder agreed well with the cubic $BaTiO_3$ structure in the *Pm*3*m* space group (JCPDS data no 31-0174). Based on XRD results, Rietveld refinement analysis gave lattice parameters of a = 4.0415±0.0004 Å, which were slightly larger than those reported to value a = 4.031 Å (JCPDS data no 31-0174). This slight expansion of lattice parameters (*a*) might be due to the presence of a trace amount of the OH group trapped in the crystal lattice, which can be confirmed by solvothermal treatment with Dimethylformamide (DMF). The intensities and positions of the peaks match very well with those data reported in the literature[15, 16]. No peaks in any other phase were detected, thus indicating high purity of the product. These results indicate that impurity of the $BaCO_3$ phase can be reduced or eliminated when the product is synthesized with a high concentration of precipitating agent (NaOH) and in the closed system with Ar atmosphere.

3.3 Effect of precursor concentration on the perovskite phase formation

The effect of Ba and Ti ion concentration in the starting solution on the perovskite phase formation was observed. The Ba ion to Ti ion ratio in the solution was kept constant at 1:1. The precursor concentration varied from 0.01 to 1.5 mol L^{-1}. Figure 3 (a) illustrates the XRD pattern of $BaZr_yTi_{1-y}O_3$; $y = 0.0$ powders at different precursor concentrations synthesized for 60 min with 20 mol L^{-1} of NaOH in Ar atmosphere. The XRD pattern displayed the $BaCO_3$ and $Ba(OH)_2(H_2O)_3$ phase at a low precursor concentration (≤ 0.1 mol L^{-1}), the perovskite phase was not observed. The perovskite phase started to form at 0.1 mol L^{-1}. When the concentration increased to 0.5 mol L^{-1}, the $BaCO_3$ peak disappeared, and the pure perovskite phase was obtained. Figures 3 (b) to (d) display the morphology of the product synthesized with different precursor concentrations. Two types of morphological particles were observed clearly at a low precursor concentration (0.01 mol.L^{-1}); i.e. a large particle with irregular morphology and small one with agglomerated form. The energy dispersive X-ray (EDX) analysis [Figure 3(b)] indicated that the large particle was the $BaCO_3$

phase, while the agglomerated cluster was the Ti-amorphous phase. The results corresponded well with the XRD pattern. The morphology of the particle changed significantly with increased precursor concentration to a more spherical shape, and a narrow size distribution was observed clearly. The histogram of particle size distribution in Figure 3 (d) illustrates nanoparticles with a narrow size distribution that ranges within the average particle dispersity (D_{SEM99}/D_{SEM50}) of 1.54. The average particle size decreased significantly with increasing precursor concentration, and when measured by SEM was found to be 123.2 ± 42.8 nm and 49.6 ± 11.2 nm for powder synthesized in 0.5 mol.L^{-1} and 1.5 mol.L^{-1} of precursor concentration, respectively. The intensity of the XRD pattern decreased when the precursor concentration increased to 1.5 mol L^{-1}, while the FWHM value was increased, thus indicating that nanocrystals tend to become smaller. The Hall-Williamson plot of $\beta_{hkl}\cos(\theta)/\lambda$ versus $4\sin\theta$ gives the value of strain from the slop of the fit, as shown in Figure 4(a-f). The crystalline size calculated from the Scherrer and Hall-Williamson methods is summarized in Table 1, where this assumption has been confirmed. The crystallite size of powder was found to be 36.61±13.96 nm and 16.40±01.46 nm when synthesized in 0.5 mol.L^{-1} and 1.5 mol.L^{-1} of precursor concentration, respectively. It is interesting to note that the particle size becomes close to the crystallite size with increasing precursor concentration, which indicates that particles synthesized at a high precursor concentration are composed of fewer crystallites. Generally, particle sizes that precipitate from solution are influenced by the relative rates of nuclei formation and crystallite growth, and a high nucleation rate can produce a large number of small crystallites [19, 44]. A larger number of cations at higher values of precursor concentration diffuse in solution, thus leading to a higher degree of supersaturation and higher nucleation rate [11, 29]. As a result, the size of the final particles decreased with increasing precursor concentration, while a large number of small crystallites were formed. The structural and morphological characterizations converged when demonstrating that the sonochemical synthesis process leads to forming the cubic $BaTiO_3$ phase, with 100-nm grade nanopowders and a narrow size distribution.

3.4 Effect of sonication time on the morphology and particle size distribution

To investigate the details of sonochemical conversion from precursor to the final perovskite phase, a series of experiments employed different sonication times, without changing the conditions of other preparations. Figure 5 (a) shows the XRD pattern of as-prepared $BaZr_yTi_{1-y}O_3$; $y = 0.0$ powders synthesized by 1 mol.L^{-1} of precursor concentration with 20 mol.L^{-1} of NaOH in Ar atmosphere at different sonication times. The pure perovskite structure was observed clearly at 5 min sonication time by using a strong base solution (20 mol.L^{-1} NaOH) and high precursor concentration ($\geq$ 0.5 mol.L^{-1}), with the powder synthesized in a closed system with Ar gas. No $BaCO_3$ phase or unwanted phase was found, but intensity of the perovskite phase was quite low. This indicated that the product had low crystallinity, which improved significantly with increasing ultrasonic irradiation time. A sharp XRD pattern was observed clearly at 60 min sonication time. Figures 5 (b) to (d) illustrate the secondary electron images of $BaZr_yTi_{1-y}O_3$; $y = 0.0$ synthesized at different sonication times. Figure 5 (b) and (c) show that nanocrystals of $BaZr_yTi_{1-y}O_3$; $y = 0.0$ were formed firstly under ultrasonic irradiation, and then readily agglomerated into aggregated particles in a short period of time, in order to minimize high surface energy. The particle size and shape of the cluster are difficult to identify. However, the spherical shape and uniformity of the particle were observed clearly with increased sonication time [Figures 5 (d) to (f)]. Sphere-like particles were achieved, evidently after 20 min sonication time, and the particle size increased slightly after 2 h under ultrasonic irradiation. The particles showed a monosized spherical shape that was different from that in other wet chemical synthesizing methods [12, 14-16]. The products had a slightly spherical morphology, and the particle size distribution was rather narrow. Furthermore, by increasing the sonication time further, the formation of neck between the particles was observed, which is caused by high velocity interparticle collision generated by ultrasonic irradiation [Figure 5 (d)]. The high velocity of interparticle collision can make surface diffusion, as the melting point starts from the surface area of nanoparticles[24]. Surface diffusion is transportation of a typical mass in the sintering mechanism that produces surface smoothing[29], particle joining[23, 45], grain boundary formation[24, 45] and neck growth[45]. Nevertheless, densification and volume shrinkage did not originate, as the sonochemical method generated local thermal energy that differed from thermal energy of the sintering process[22].

3.5 *Effect of the Zr/Ti molar ratio on the perovskite phase formation*

The evolution of XRD patterns of $BaZr_yTi_{1-y}O_3$; $y = 0.0$, 0.2, 0.4 and 0.6 powders synthesized in different sonication times is shown in Figures 6 (a) to (d). Strong influence of the Zr/Ti ratio was observed clearly on perovskite phase formation, which started for the composition, $y = 0.0$, at 5 minutes sonication time [Figure 6 (a)]. Otherwise, formation of the perovskite phase started to form at 10 and 15 minutes sonication time for the composition, $y = 0.2$ and 0.4, respectively [Figure6 (b) and (c)]. However, as shown in Figure 6 (d), no strong crystal phases can be found from the XRD pattern for the composition, $y = 0.6$, meaning that the samples were composed of an amorphous phase, of which its formation might be related to different regions of sonochemical activity. Two regions of sonochemical activity are known to exist, as postulated by Suslick and co-workers [22, 46]. One is the inside of collapsing bubbles and the other the interfacial region between the cavitation bubbles and surrounding solution. The inside of collapsing bubbles generates extremely high temperature (>5,000 K), pressure (>20 MPa) and very high cooling rates (excess of 10^{10} K/s), whereas the interfacial region generates a much lower temperature, which is still high enough to rupture chemical bonds and induce a variety of reactions [45]. When a reaction takes place inside collapsing bubbles, the final product is amorphous, as a result of the extremely rapid cooling rate (>10^{10} K/s) that occurs during the collapse. Conversely, if a reaction occurs within the interfacial region, nanocrystalline products are expected to materialize. Since amorphous powders were obtained in this study at a high Zr/Ti ratio, the authors postulate that the formation of Ba(Zr/Ti)O_3 at a high and low Zr/Ti ratio probably occurs inside and at the interfacial region of collapsing bubbles, respectively. Similar behavior was observed in stibnite (Sb_2S_3) nanorod that was synthesized by the sonochemical method [47]. Besides, another factor might relate to the difference in formation constant of the complex metallic hydroxide network. At a high Zr concentration, hetero-trimetallic Ba-Ti-Zr-hydroxide may have difficulty in forming a network [44]. All compositions of powders synthesized at 60 min sonication time were selected in order to investigated the solid solution and identify the crystal structure. The XRD pattern of $BaZr_yTi_{1-y}O_3$; y = 0.0, 0.2, and 0.4 nanoparticles, synthesized for 60 min sonication time are presented in Figure 7(a). All powders exhibit a pure perovskite structure without a trace of impurity, indicating that Zr^{4+} has diffused into the host lattice to form a solid solution. One symmetric peak observed at $2\theta \sim 44^o$ to 46^o in all of the samples confirmed that all compositions had a cubic symmetry. This agreed well with previous reports that used the co – precipitation method [16]. Additionally, the XRD pattern demonstrated a progressive peak shift toward the lower diffraction angle with increased Zr^{4+} [Figure 7(b)]. This phenomenon can be explained qualitatively with respect to the unit cell volume caused by the substitution of Zr^{4+} at the Ti-site. According to Shannon's effective ionic radii, with a coordination number of 6, the ionic radius of B-site ions (Zr^{4+}) is 0.86 Å, which is close to the radius of Ti^{4+} (0.745 Å)[48]. The calculated lattice parameters (a) and unit cell volume (v) of $BaZr_yTi_{1-y}O_3$; y = 0.0, 0.2, and 0.4 powders are reported in Table 2. These values increase with increased Zr content by replacing Ti^{4+}- site (0.745 Å) with large Zr^{4+} (0.86Å) ions. The Raman spectra are shown clearly in Figure 7(c). All Raman peaks of the composition y = 0.00, 0.20 and 0.40 were observed similarly. The 4 broadening peaks at around 186, 303, 522 and 715 cm^{-1} are assigned to the [A_1(TO) + E(LO)], [A_1(TO)], [E, A_1(TO)] and [A_1, E(LO)] Raman-active modes of tetragonal (*P*4*mm*) symmetry [49]. It is noteworthy that despite the XRD data [Figure 7(a)] showing the cubic (P*m*3*m*) symmetry, the Raman spectra show the tetragonal (*P*4*mm*) crystal structure. This is because of the hydroxyl defect from a high basic environment. The -OH groups can substitute the sub-lattice to form a metastable cubic phase. However, the hydroxyl defect existed as interstitial defects in many unit cells, but not all. Therefore, some unit cells can stabilize in a tetragonal structure. Nevertheless, characterization by XRD gives results in a static and average symmetry, while the result in a dynamic and local symmetry could be characterized by Raman spectroscopy [49]. Therefore, the results from Raman did not correlate with those from XRD data in this situation. In fact, the crystal structure of powder products may exhibit a mixture between the tetragonal and cubic crystal structure. However, the hydroxyl defects could be removed by chemical treatment with DMF, which is discussed later. Furthermore, Figure 7(c) also reveals that all of the Raman peaks disappeared when the composition (*y*) of the Zr/Ti ratio was increased to 0.60. The presence of a very broad hump demonstrated a predominantly amorphous phase characteristic. This result confirms that the condition of powder products was stabilized in the amorphous phase. Furthermore, the FT-IR spectrum of powder products at various Zr/Ti ratios was studied and reported in Figure 7(d). The band appearing for all compositions at around 3,600 and 1,600 cm^{-1} is attributed to O-H stretching and O-H bending vibration, respectively. In corresponding with previous results, it could be said that the OH vibration bands in the 0.00 - 0.40 compositions of the Zr/Ti ratios come from the OH-defects, that existed on the surface particles and in the sub-lattice. On the other hand, the O-H vibration band in the 0.60 composition of the Zr/Ti ratio may come from the mixture between OH^- species defects and -OH groups from the amorphous phase. In addition, the absorption peak at around 520 cm^{-1} was used to indicate the difference of trimetallic Ba-Ti-Zr hydroxides amorphous and crystalline BZT phases. This peak is assigned mainly to the characteristic peak of the perovskite structure, while associating with the absorption vibration of Ti-O and Zr-O asymmetric stretching in BO_6 octahedra[14, 50]. The 0.00-0.40 compositions showed the strong of asymmetric stretching in BO_6 octahedra, thus confirming that the powder products in these conditions were formed as BZT solid solution without the impurity or the other phases. Interestingly, the BO_6 vibration band disappeared at the 0.60 composition of the Zr/Ti ratio, while the OH absorption band exhibited large intensity, thus suggesteing that the BZT solid-solution phase was not found at this condition. Therefore, it can be confirmed that the product powder may stabilize in the form of trimetallic Ba-Ti-Zr hydroxides in the amorphous phase. The SEM/EDX analysis at different points on the surface of individual particles was performed in order to confirm the homogeneity of the powder products. Figure 5(e) and (f) display the EDX spectra at different points on the surface of individual particles. It can be seen from these figures that the concentrations of various elements (Ba, Ti, Zr and O) involved in the individual particle are very close to each other indicating to the homogeneity of the powder products. The result from SEM/EDX spectra showed good correspondence with the result from XRD [Figure 7(a)]. This observation clearly demonstrates that the multicationic perovskite $BaZr_yTi_{1-y}O_3$; $y = 0.0 - 0.4$ solid solution was formed completely during the sonochemical process itself, without the need for further calcination or a heating process.

3.6 Effect of chemical treatment on the crystal structure by using dimethyl formamide (DMF)

Ordinarily, hydroxyl (-OH) groups play an important role in the synthesis of perovskite nanopowders via wet-chemical processes, especially in a very high OH concentration (pH > 12) [20, 49-53]. The powder products can contain much chemical bonding with the two types of OH species. Weakly bonded OH^- species are adsorbed on particle surfaces, while strongly bonded OH^- species are entrapped in the crystal lattice, to form lattice OH^- defects [20]. These defects can affect the stability of lattice vibration and decrease tetragonality to form a metastable cubic phase, which leads to the absence of phase transition [20]. From the literature, the OH^- species on particle surfaces could be eliminated by thermal heat treatment above 300°C, and above 1,100°C for eliminating the lattice OH^- species [20, 52, 53]. This work investigated sonochemical $Ba(Zr_yTi_{1-y})O_3$ powder products and found hydroxyl defects similar to those in the $BaTiO_3$ reported in the literature [20, 53]. Nevertheless, in this work, lattice hydroxyl defects could be removed completely by solvothermal treatment with DMF solution at only 170°C. In studying the effect of DMF on the crystal structure, a selected region of XRD patterns in $2\theta = 42^{\circ}$ to 48° of $Ba(Zr_yTi_{1-y})O_3$ ($y = 0.00$) powder products was compared between before and after treatment, as shown in Figure 8 (a). The results clearly show the difference of tetragonal versus cubic crystal structure. Before treatment, the powder products showed a single peak of (200) reflection, which agreed well with the characteristic of a cubic crystal structure. When the powder products were treated with DMF solution at 170°C for 24 h, splitting of (200) reflected at a higher region, with a (002) shoulder at the lower region, and this corresponded to the characteristics of a tetragonal crystal structure. In accordance with a large amount of lattice OH^-, a high amount of protons (H^+) can link and exist in an oxygen sub-lattice. Therefore, the unit cell volume was enlarged with close correlation, and distortion of the tetragonal crystal structure was observed. Consequently, a cubic crystal structure was presented [20]; then, when the lattice OH^- was removed, the tetragonal structure returned to stabilize it. FT-IR spectroscopy was used to investigate the functional group of $Ba(Zr_yTi_{1-y})O_3$ ($y = 0.00$) powders. The spectrum is shown in Figure 8(b). O-H stretching vibration of the hydroxyl group and $Ti\text{-}O_6$ stretching vibration of in BO_6 octahedra of $BaTiO_3$ were detected on $Ba(Zr_yTi_{1-y})O_3$ ($y = 0.00$) powders before treatment. Then, the band of O-H stretching disappeared, while TiO_6-stretching was still present after the treatment process. It could be seen that the hydroxyl species were desorbed more effectively after the treatment process. However, it is difficult to distinguish between the surfaced-adsorbed and lattice hydroxyl groups because the peak position of two OH^- species is very similar [52, 53]. Furthermore, Raman scattering spectroscopy also was studied for further investigation. The Raman spectra of $Ba(Zr_yTi_{1-y})O_3$ (y = 0.00) compared before and after chemical treatment are shown in Figure 8 (c). All Raman-active modes in the powder products after chemical treatment clearly correspond to those in the $4E(TO + LO) + 3A_1(TO + LO) + B_1(TO + LO)$ of a tetragonal ($P4mm$) crystal structure [49]. However, there are 3 broadening peaks at around 303, 522 and 715 cm^{-1} in powder products before treatment, which are assigned to the Raman-active modes of tetragonal ($P4mm$) symmetry, indicating that the crystal structure of powder products before treatment may exhibit a mixture between tetragonal and cubic crystal structure. However, when the chemical treatment was preceded by DMF, the cubic crystal structure changed completely to be tetragonal. In addition, it is well known that the existence of OH^- defects leads to loss of phase transition in ferroelectric materials [49, 50]. Therefore, DSC measurement was used for further investigation of $Ba(Zr_yTi_{1-y})O_3$ (y = 0.00) phase transition. The DSC data are shown in Figure 8 (d). The powder products before treatment show only the baseline, without the change of enthalpy (ΔH), while those after treatment clearly show the exothermic transition on cooling at temperatures of about 127.1°C, which correlates to the phase transition temperature of tetragonal to cubic crystal structure. The relating change in enthalpy (ΔH) value of this transformation is 593 mJ/g, which corresponds to 650 mJ/g of the commercial $BaTiO_3$ tetragonal structure. On the other hand, the Curie temperature observed from DSC data can be used to confirm the 1:1 stoichiometry Ba/Ti ratio in $Ba(Zr_yTi_{1-y})O_3$ (y = 0.00) powder products, which is similar to reports from F. Baeten [51]. Finally, all the results from this part of this study indicate that the use of chemical treatment with DMF solution possibly eliminates OH^- defects from the oxygen sub-lattice. The tetragonal crystal structure was improved, and the phase transition observed at 127^{o}C. In addition, the chemical treatment with DMF had no significant effect on the particle shape, size or size distribution. The particle size changed slightly from 97.4 ± 19.2 nm to 103.5 ± 13.3 nm with a narrow size distribution. The SEM micrographs of powder products before and after chemical treatment are shown in Figure 8 (e) and (f), respectively.

3.7 Mechanism of crystal growth formation

Based on the results achieved with different synthetic parameters, perovskite phase formation of the $BaZrTiO_3$ spheres involved the crystallization process and was similar to mechanical stirring [54]. A plausible mechanism that explains all these data is shown in Figure 9. The first stage of the synthesis is forming a complex network of the amorphous phase, which is assumed to be flows: i.e. barium cations that form $\mathrm{Ba(OH)^+}$ species in the NaOH concentration. Furthermore, titanium and zirconium cations were hydrolyzed readily in NaOH solutions to form soluble $\mathrm{[Ti(OH)_6]^{2-}}$and $\mathrm{[Zr(OH)_5]^-}$anions. The formation of hexahydraxy titanate(IV) and pentahydraxy zirconate (IV) $\mathrm{[Zr(OH)_5]^-}$ in the presence of strong alkaline condition were described also by N.C Pramanik *et al* [42] and Boshini *et al* [55] respectively. The reaction between $\mathrm{Ba(OH)^+}$, $\mathrm{[Ti(OH)_6]^{2-}}$and $\mathrm{[Zr(OH)_5]^-}$ initiated the formation of gels comprising an entangled complex network of polymeric chains of trimetallic Ba-Ti-Zr hydroxides. The skeleton of the polymer corresponds to the Ba, Ti and Zr atom linked by bridging O atoms. The second stage of the synthesis is accelerating the formation of tiny primary BZT particulates (crystallization) by ultrasonic irradiation. The results presented in a previous section of this study strongly indicate that formation of BZT is dominated by a nucleation and growth mechanism. When the complex network of amorphous phases was irradiated ultrasonically, the formation, growth, and implosive collapse of bubbles (microjet effect) in liquid medium generated extreme synthesis conditions (localized hot spot with high temperature of ca. 5,000 K, pressure of ca. 20 MPa, and a very high cooling rate of ca. 10^{10}K S^{-1}). Also, due to vaporization of the solvent into bubbles, solubility of the reactants was enhanced, thus elevating supersaturation of the reactant solutions. In the conventional crystallization process from a solution, two steps are involved; nucleation and crystal growth, of which both have supersaturation as a common driving force. Crystals in the supersaturated solution can neither form nor grow. The nucleation rate in the crystallization process is small and only few nuclei can be generated at the initial time of growth. Then, nuclei grow in spatial orientations fixed by solute crystallized structures. However, nucleation in the sonocrystallization process was accelerated by the implosive collapse of bubbles, while the crystal growth process was inhibited or delayed by shock waves and turbulent flow created by ultrasonic radiation [22, 29]. This effect promoted nucleation over grain growth to form tiny primary particulates (crystalline), which tended to aggregate into large particles due to tremendous surface energy; and stability of the particles can be expressed as: [56, 57]

$$S = (R_a + R_b)\int_{R_a - R_b}^{\infty} \exp\left[\frac{V(C)}{k_B T}\right]\frac{dC}{C^2} \qquad (5)$$

where S is the stability factor of the particles, R_a and R_b are the radius of the two particles, respectively, $V(C)$ is the function of potential energy interaction, C is the distance between the two particles, k_B is Boltzmann's constant (1.3806 x 10^{-23} J.K^{-1}) and T is the temperature (K). When the distance between particles is decreased to a certain extent, short-range reactions (van der Waal's forces and existence of an electrostatic barrier) lead to strong attraction between particles [56, 57]. The third stage of synthesis is forming spherical particles with a narrow size distribution. The turbulent flow and mechanical effects, such as microjet impact and shock waves that generate from the implosive collapse of bubbles under ultrasonication[24, 46], can create a relatively uniform reaction in fluid medium[24, 46], which improves the spherical shape of monodispersed BZT particles. Microjets with a high velocity of over 400 km/h crush the aggregated cluster in all directions [21, 43], and nanocrystalline particles are driven together at extremely high speeds, thus inducing effective melting at the point of impact [22, 45]. These phenomena generate relatively monodispersed particles with a narrow size distribution. Furthermore, when increasing the sonication time further, neck formation was observed between the particles, caused by high velocity of the interparticle collision generated by ultrasonic irradiation [45]. Suslick *et.al.* [45, 46] proposed that the effects of cavitation in the phenomenon of interparticle collisions come from the shock waves released into liquid and not from the temperature of the localized hot-spot formed within the collapsing bubble. It is interesting to note that volume shrinkage and densification did not originate, due to the sonochemical method that generated local thermal energy, which differed from thermal energy of the sintering process.

4. Conclusion

Multicationic oxides based on the complex perovskite structure of $Ba(Zr_yTi_{1-y})O_3$;$y = 0.0$-0.4 nanoparticles were synthesized directly under ultrasonic irradiation in the sonochemical synthesis process, without a calcination step. The concentration of NaOH, the precursor and synthesized atmosphere play a key role in forming the perovskite structure. Strong and high concentration of NaOH and the precursor, respectively, not only initiate nucleation, but also eliminate the formation of $BaCO_3$. Nanocrystalline was formed in a short period of time and then aggregated to form large particles. Narrow size distribution was acquired for the aggregated particles under ultrasonic irradiation. However, the synthesized powder had some of the OH group trapped in the crystal lattice, which was caused by strong OH concentration during the synthesis process. A plausible crystal growth mechanism was proposed by this study.

Acknowledgement

This work was supported by the Thailand Research Fund (TRF) under grant. No BRG5680006 and S. Wirunchit would like to thank The Royal Golden Jubilee (RGJ-Ph.D program) Scholarship program for financial support.

5. References

1. X. G. Tang, K. H. Chew and H. L. W. Chan, *Acta Materialia*, 2004, **52**, 5177-5183.
2. W. Liu and X. Ren, *Physical Review Letters*, 2009, **103**.
3. L. Zhang, M. Zhang, L. Wang, C. Zhou, Z. Zhang, Y. Yao, L. Zhang, D. Xue, X. Lou and X. Ren, *Applied Physics Letters*, 2014, **105**.
4. H. Guo, B. K. Voas, S. Zhang, C. Zhou, X. Ren, S. P. Beckman and X. Tan, *Physical Review B - Condensed Matter and Materials Physics*, 2014, **90**.
5. J. Bera and S. K. Rout, *Materials Letters*, 2005, **59**, 135-138.
6. A. J. Moulson and J. M. Herbert, *Electroceramics: Materials, Properties, Applications*, Wiley, 2003.
7. M. Sopicka-Lizer, *High-Energy Ball Milling: Mechanochemical Processing of Nanopowders*, Elsevier Science, 2010.
8. X. Hou and J. Yu, *Journal of the American Ceramic Society*, 2013, **96**, 2218-2224.
9. A. S. Bhalla, R. Guo and R. Roy, *Mat. Res. Innovat.*, 2000, **4**, 3.
10. G. H. Haertling, *Journal of the American Ceramic Society*, 1999, **82**, 797-818.
11. J. S. Reed, *Principles of Ceramics Processing*, Wiley, 1995.
12. P. Julphunthong and T. Bongkarn, *Current Applied Physics*, 2011, **11**, S60-S65.
13. N. Binhayeeniyi, P. Sukvisut, C. Thanachayanont and S. Muensit, *Materials Letters*, 2010, **64**, 305-308.
14. M. Veith, S. Mathur, N. Lecerf, V. Huch, T. Decker, H. P. Beck, W. Eiser and R. Haberkorn, *Journal of Sol-Gel Science and Technology*, 2000, **17**, 145-158.
15. J. Q. Qi, Y. Wang, W. P. Chen, L. T. Li and H. L. W. Chan, *J Nanopart Res*, 2006, **8**, 959-963.
16. S. B. Reddy, K. P. Rao and M. S. R. Rao, *Scripta Materialia*, 2007, **57**, 591-594.
17. Z. L. Wang and J. Song, *Science*, 2006, **312**, 242-246.
18. X. Wang, J. Song, J. Liu and L. W. Zhong, *Science*, 2007, **316**, 102-105.

19. D. Segal, *Chemical Synthesis of Advanced Ceramic Materials*, Cambridge University Press, 1991.
20. P. K. Dutta, R. Asiaie, S. A. Akbar and W. Zhu, *Chemistry of Materials*, 1994, **6**, 1542-1548.
21. K. J. Leonard, S. Sathyamurthy and M. P. Paranthaman, *Chemistry of Materials*, 2005, **17**, 4010-4017.
22. J. H. Bang and K. S. Suslick, *Advanced Materials*, 2010, **22**, 1039-1059.
23. J. Janbua, J. Mayamae, S. Wirunchit, R. Baitahe and N. Vittayakorn, *RSC Advances*, 2015, **5**, 19893-19899.
24. K. S. Suslick, *Science*, 1990, **247**, 1439-1445.
25. B. Zhou, B. Liu, L.-P. Jiang and J.-J. Zhu, *Ultrasonics Sonochemistry*, 2007, **14**, 229-234.
26. I. Haas, S. Shanmugam and A. Gedanken, *The Journal of Physical Chemistry B*, 2006, **110**, 16947-16952.
27. C. Wu, B. P. Mosher and T. Zeng, *Chemistry of Materials*, 2006, **18**, 2925-2928.
28. L.-P. Jiang, S. Xu, J.-M. Zhu, J.-R. Zhang, J.-J. Zhu and H.-Y. Chen, *Inorganic Chemistry*, 2004, **43**, 5877-5883.
29. H. Xu, B. W. Zeiger and K. S. Suslick, *Chemical Society Reviews*, 2013, **42**, 2555-2567.
30. D. Ghanbari, M. Salavati-Niasari and M. Ghasemi-Kooch, *Journal of Industrial and Engineering Chemistry*, 2014, **20**, 3970-3974.
31. F. Dang, K. Kato, H. Imai, S. Wada, H. Haneda and M. Kuwabara, *Ultrasonics Sonochemistry*, 2010, **17**, 310-314.
32. S. Vuttivong, S. Niemcharoen, P. Seeharaj, W. C. Vittayakorn and N. Vittayakorn, *Ferroelectrics*, 2013, **457**, 44-52.
33. M. Xu, Y. N. Lu, Y. F. Liu, S. Z. Shi, T. S. Qian and D. Y. Lu, *Powder Technology*, 2006, **161**, 185-189.
34. K. Yasui, T. Tuziuti and K. Kato, *Ultrasonics Sonochemistry*, 2011, **18**, 1211-1217.
35. P. Charoonsuk, R. Baitahe, W. Vittayakorn, N. Atiwongsangthong, R. Muanghua, P. Seeharaj and N. Vittayakorn, *Ferroelectrics*, 2013, **453**, 54-61.
36. T. Hyeon, M. Fang and K. S. Suslick, *Journal of the American Chemical Society*, 1996, **118**, 5492-5493.
37. J. Geng, L. Jiang and J. Zhu, *Sci. China Chem.*, 2012, **55**, 2292-2310.

38. S. Singh, N. Kumar, R. Bhargava, M. Sahni, K. D. Sung and J. H. Jung, *Journal of Alloys and Compounds*, 2014, **587**, 437-441.

39. Y. Han, D. Radziuk, D. Shchukin and H. Moehwald, *Journal of Materials Chemistry*, 2008, **18**, 5162-5166.

40. Y. Waseda, E. Matsubara and K. Shinoda, *X-Ray Diffraction Crystallography: Introduction, Examples and Solved Problems*, Springer, 2011.

41. C. Suryanarayana and G. Norton, *X-Ray Diffraction: A Practical Approach*, Springer, 1998.

42. N. C. Pramanik, S. I. Seok and B. Y. Ahn, *Journal of Colloid and Interface Science*, 2006, **300**, 569-576.

43. M. M. Lencka and R. E. Riman, *Ferroelectrics*, 1994, **151**, 159-164.

44. Pankaj, in *Theoretical and Experimental Sonochemistry Involving Inorganic Systems*, ed. M. Ashokkumar, Springer Netherlands, 2011, pp. 213-271.

45. T. Prozorov, R. Prozorov and K. S. Suslick, *Journal of the American Chemical Society*, 2004, **126**, 13890-13891.

46. W. B. McNamara, Y. T. Didenko and K. S. Suslick, *Nature*, 1999, **401**, 772-775.

47. H. Wang, Y.-N. Lu, J.-J. Zhu and H.-Y. Chen, *Inorganic Chemistry*, 2003, **42**, 6404-6411.

48. R. D. Shannon, *Acta. Cryst.*, 1976, **A32**, 751.

49. T. Noma, S. Wada, M. Yano and T. Suzuki, *Journal of Applied Physics*, 1996, **80**, 5223-5233.

50. S. Wada, T. Tsurumi, H. Chikamori, T. Noma and T. Suzuki, *Journal of Crystal Growth*, 2001, **229**, 433-439.

51. F. Baeten, B. Derks, W. Coppens and E. van Kleef, *Journal of the European Ceramic Society*, 2006, **26**, 589-592.

52. M. H. Frey and D. A. Payne, *Physical Review B - Condensed Matter and Materials Physics*, 1996, **54**, 3158-3168.

53. R. Kota and B. Lee, *J Mater Sci: Mater Electron*, 2007, **18**, 1221-1227.

54. A. Testino, M. T. Buscaglia, V. Buscaglia, M. Viviani, C. Bottino and P. Nanni, *Chemistry of Materials*, 2004, **16**, 1536-1543.

55. F. Boschini, A. Rulmont, R. Cloots and B. Vertruyen, *Journal of the European Ceramic Society*, 2009, **29**, 1457-1462.

56. K. S. Birdi, *Handbook of Surface and Colloid Chemistry, Third Edition*, CRC Press, 2008.

57. W. B. Russel, D. A. Saville and W. R. Schowalter, *Colloidal Dispersions*, Cambridge University Press, 1992.

Figure Legends

Figure 1	XRD patterns of $BaZr_yTi_{1-y}O_3$; $y = 0.0$ powders evolved for 60 min at various NaOH concentrations in the open air system.
Figure 2	XRD patterns of $BaZr_yTi_{1-y}O_3$; $y = 0.0$ powders obtained after sonication for 5 to 60 min in 20 $mol.L^{-1}$ of NaOH concentrations in the (a) open air system and (b) closed system with Ar gas.
Figure 3	XRD pattern (a) and SEM images (b) to (d) of $BaZr_yTi_{1-y}O_3$; $y = 0.0$ powders synthesized for 60 min at various precursor concentrations in 20 mol L^{-1} of NaOH in Ar atmosphere.
Figure 4	Hall-Williamson plot (a) $y = 0.0$ at 0.5 $mol.L^{-1}$of precursor concentration (b) $y = 0.0$ at 1 $mol.L^{-1}$ of precursor concentration (c) $y = 0.0$ at 1.5 $mol.L^{-1}$ of precursor concentration, (d) $y = 0.05$, (e) $y = 0.2$ and (f) $y = 0.4$.
Figure 5	XRD pattern (a) and SEM images (b) to (e) of $BaZr_yTi_{1-y}O_3$; $y = 0.0$ powders synthesized at various reaction durations in 20 mol L^{-1} of NaOH in Ar atmosphere.
Figure 6	XRD patterns of $BaZr_yTi_{1-y}O_3$; $y = 0.0$, 0.2, 0.4 and 0.6 powders synthesized at various sonication times in 20 mol L^{-1} of NaOH solutions (a) $y = 0.0$ (b) $y = 0.2$, (c) $y = 0.4$ and (d) $y = 0.6$.
Figure 7	XRD patterns of $BaZr_yTi_{1-y}O_3$; $y = 0.0$, 0.2 and 0.4 powders synthesized at 60 min sonication time (a) Enlarged ranges of 28-34^o (b) Raman spectrum (c) and FT-IR spectrum (d) SEM/EDX results of the composition $y = 0.4$ powders (e and f).
Figure 8	XRD pattern (a), FT-IR (b), Raman (c), DSC (d) and SEM image of $BaZr_yTi_{1-y}O_3$; $y = 0.0$ untreated powders (e) and chemically treated powders with DMF (f).
Figure 9	Schematic diagrams illustrating formation of the crystal growth mechanism.

Table Headings

Table 1 Crystalline size (D) and lattice strain calculations of the $BaZr_yTi_{1-y}O_3$; $y = 0.0$, 0.05, 0.2 and 0.4 powders as determined by X-ray diffraction

Table 2 Lattice parameter (*a*), and unit cell volume (*v*) of the $BaZr_yTi_{1-y}O_3$; $y = 0.0$, 0.2 and 0.4 powders as determined by X-ray diffraction

Table 1 Crystalline size (D) and lattice strain calculations of the $BaZr_yTi_{1-y}O_3$; y = 0.0, 0.05, 0.2 and 0.4 powders as determined by X-ray diffraction

Sample		Scherrer method	Hall-Williamson method		SEM
y	Conc. (mol.L^{-1})	Crystalline size (nm)	Crystalline size (nm)	ε (× 10^{-3})	Particle size (nm)
0.00	0.50	36.6 ± 13.9	28.5	2.01 ± 0.002	123.2 ± 42.8
0.00	1.00	28.8 ± 09.4	26.4	2.68 ± 0.001	93.0 ± 28.2
0.00	1.50	16.4 ± 01.4	15.0	1.53 ± 0.003	49.6 ± 11.2
0.05	1.00	29.8 ± 07.4	18.6	3.87 ± 0.002	96.3 ± 14.0
0.20	1.00	33.2 ± 12.7	19.1	3.56 ± 0.003	108.1 ± 19.3
0.40	1.00	33.5 ± 12.3	19.4	3.55 ± 0.002	115.5 ± 11.0

Table 2 Lattice parameter (*a*), and unit cell volume (*v*) of the $BaZr_yTi_{1-y}O_3$; y = 0.0, 0.2 and 0.4 powders as determined by X-ray diffraction

Sample		Lattice Parameters (*a*)	Unit cell volume (*v*)
y	Conc. (mol·L^{-1})	(Å)	(Å)^3
0.00	1.00	4.0415 ± 0.0004	65.42
0.20	1.00	4.0641 ± 0.0004	67.12
0.40	1.00	4.0931 ± 0.0011	68.57

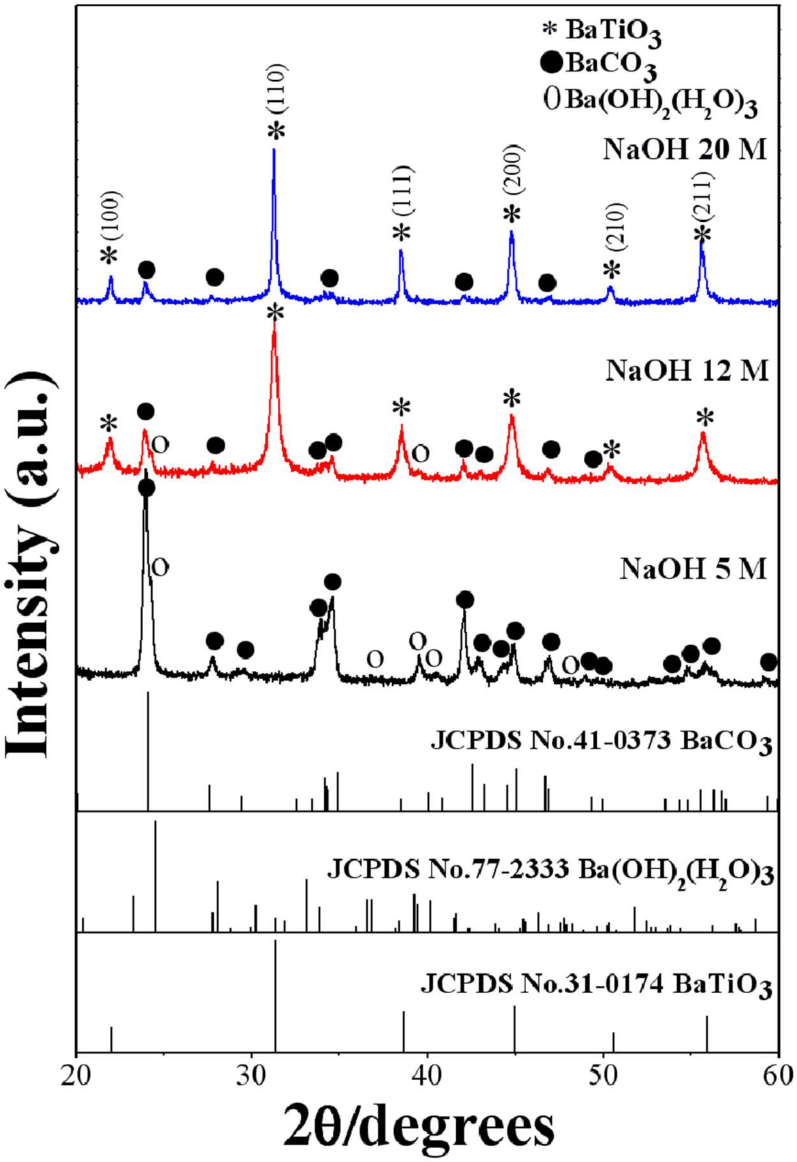

Figure 1 XRD patterns of BaZryTi1−yO3; y = 0.0 powders evolved for 60 min at various NaOH concentrations in the open air system.
76x110mm (300 x 300 DPI)

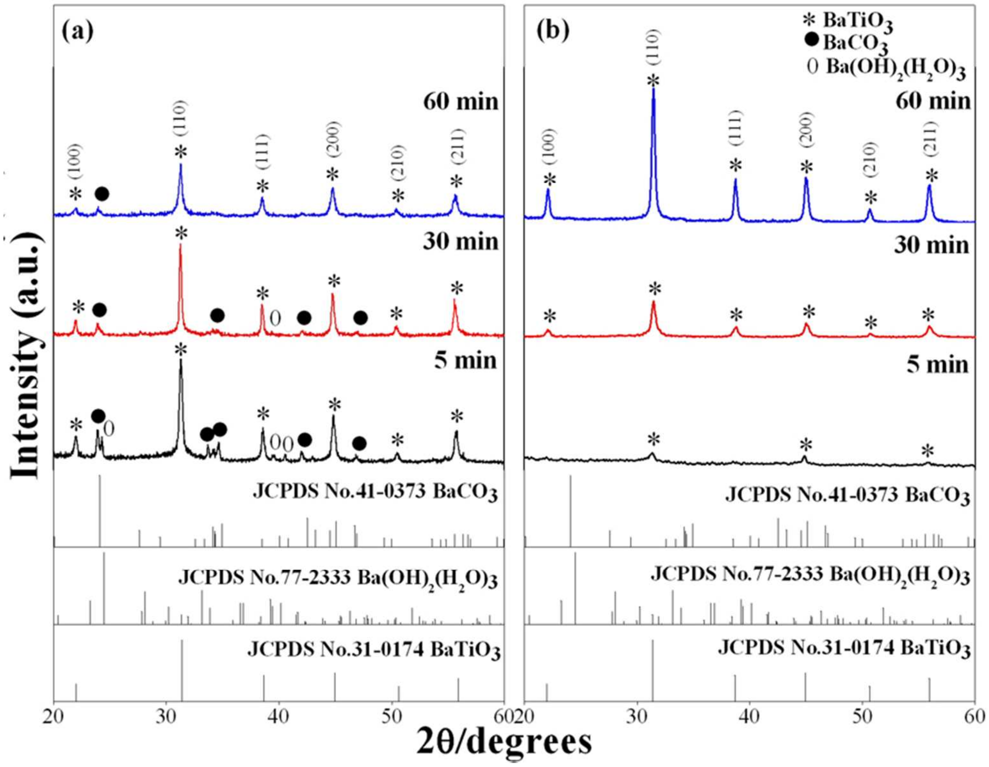

Figure 2 XRD patterns of BaZryTi1−yO3; y = 0.0 powders obtained after sonication for 5 to 60 min in 20 mol.L-1 of NaOH concentrations in the (a) open air system and (b) closed system with Ar gas.
76x58mm (300 x 300 DPI)

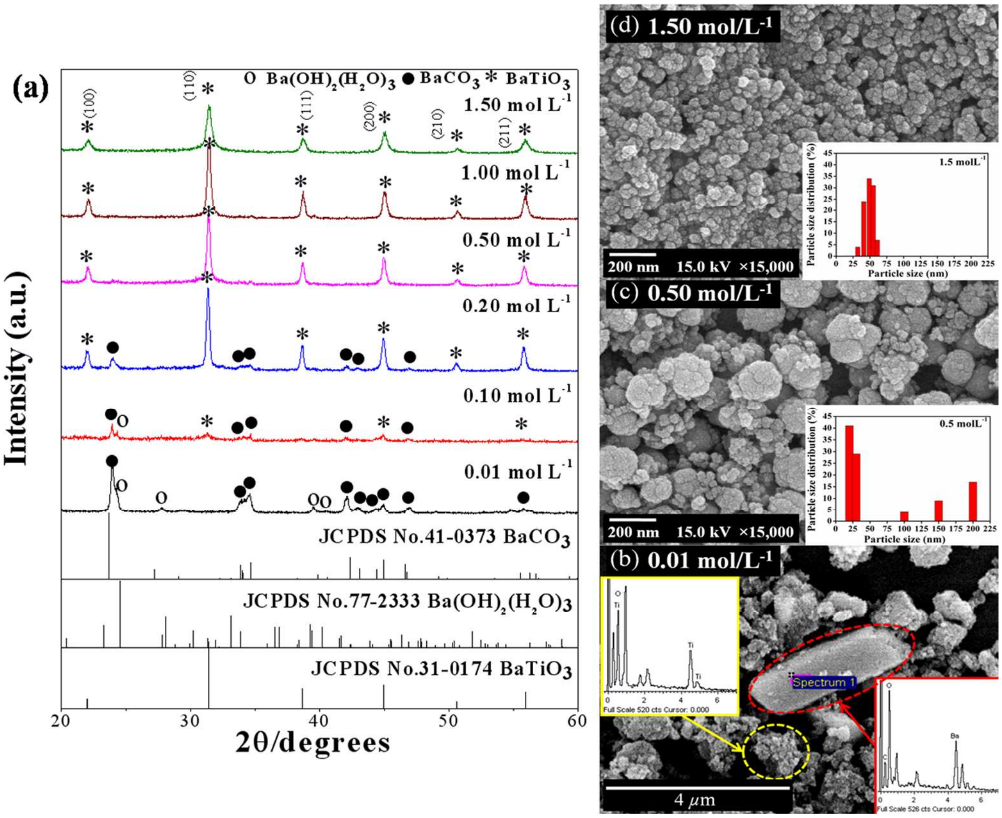

Figure 3 XRD pattern (a) and SEM images (b) to (d) of BaZryTi1−yO3; y = 0.0 powders synthesized for 60 min at various precursor concentrations in 20 mol L-1 of NaOH in Ar atmosphere.
139x113mm (300 x 300 DPI)

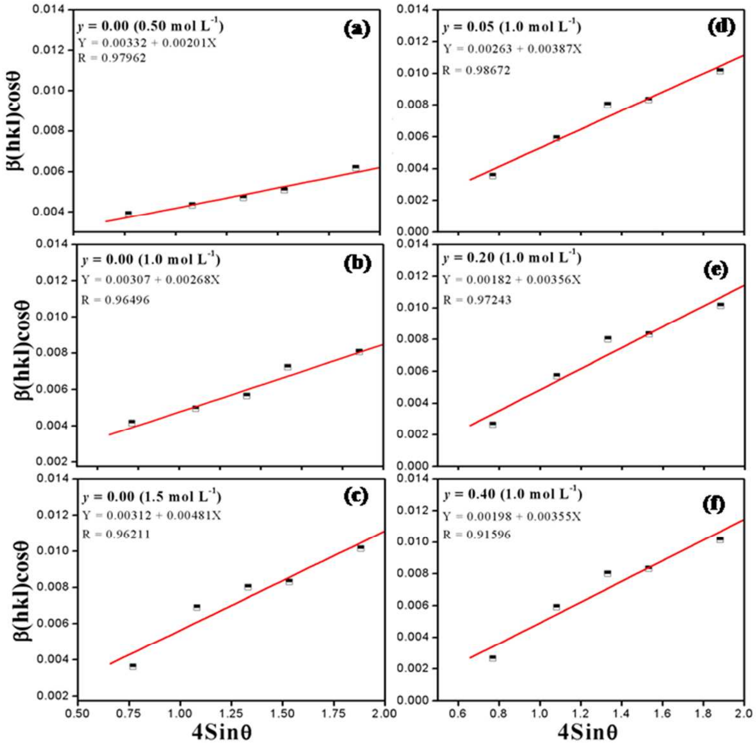

Figure 4 Hall-Williamson plot (a) y = 0.0 at 0.5 mol.L-1of precursor concentration (b) y = 0.0 at 1 mol.L-1 of precursor concentration (c) y = 0.0 at 1.5 mol.L-1 of precursor concentration, (d) y = 0.05, (e) y = 0.2 and (f) y = 0.4.
127x95mm (300 x 300 DPI)

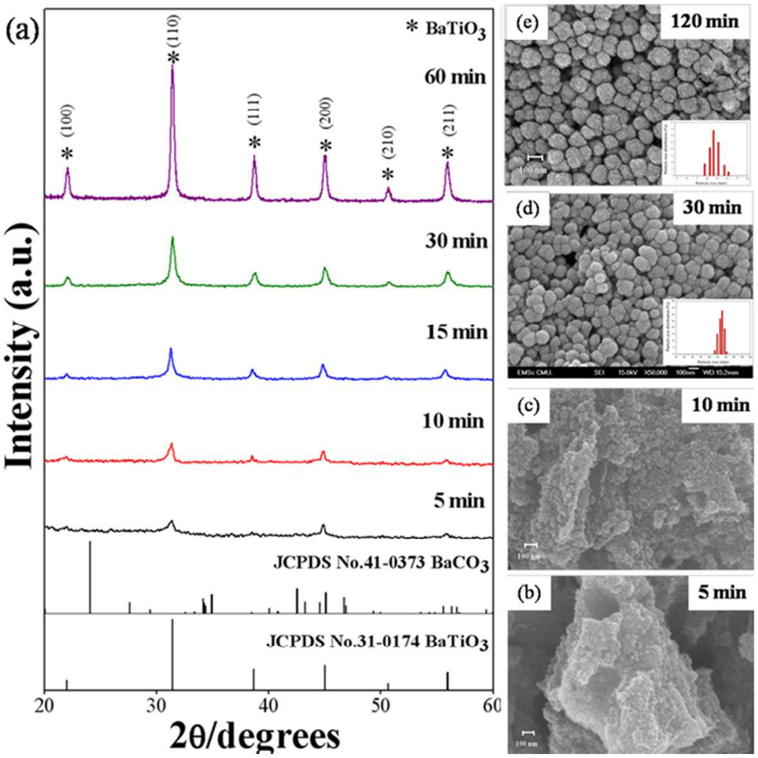

Figure 5 XRD pattern (a) and SEM images (b) to (e) of BaZryTi1−yO3; y = 0.0 powders synthesized at various reaction durations in 20 mol L-1 of NaOH in Ar atmosphere.
101x76mm (300 x 300 DPI)

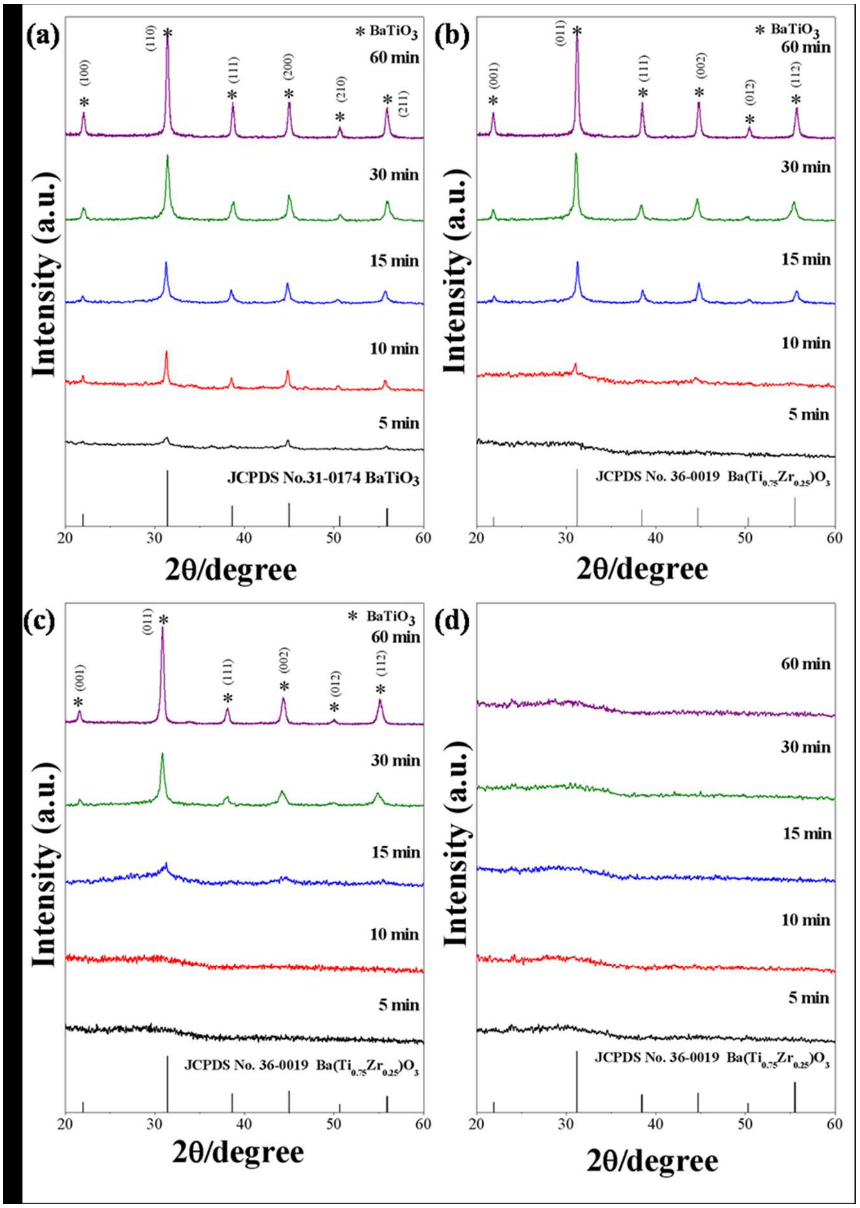

Figure 6 XRD patterns of BaZryTi1−yO3; y = 0.0, 0.2, 0.4 and 0.6 powders synthesized at various sonication times in 20 mol L-1 of NaOH solutions (a) y = 0.0 (b) y = 0.2, (c) y = 0.4 and (d) y = 0.6.
76x107mm (300 x 300 DPI)

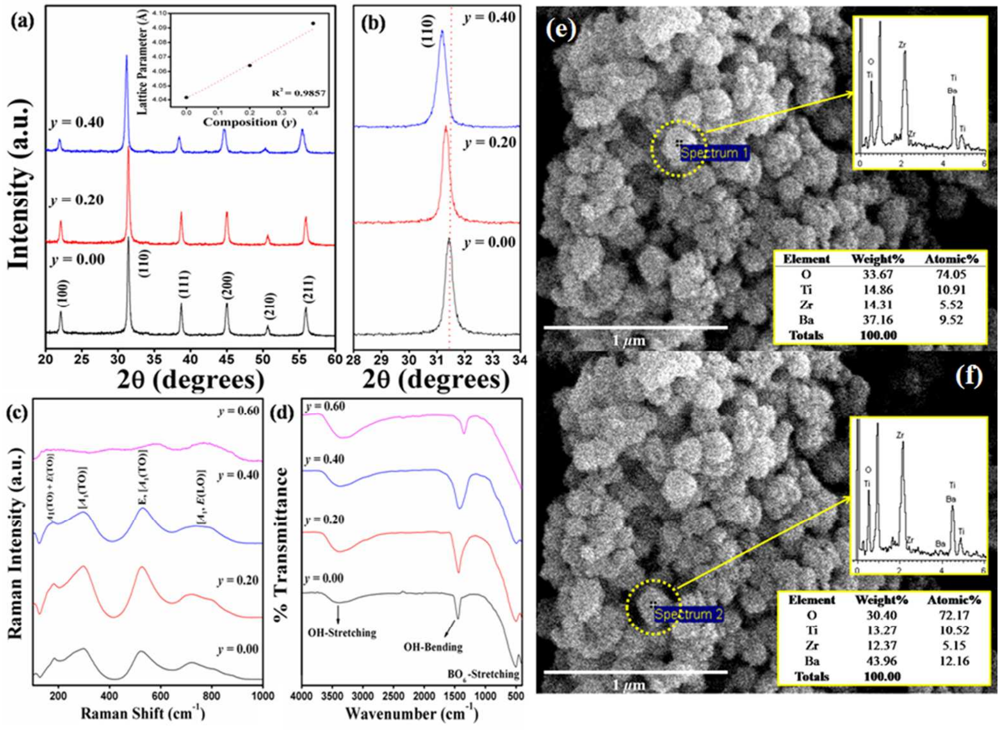

Element	Weight%	Atomic%
O	33.67	74.05
Ti	14.86	10.91
Zr	14.31	5.52
Ba	37.16	9.52
Totals	100.00	

Element	Weight%	Atomic%
O	30.40	72.17
Ti	13.27	10.52
Zr	12.37	5.15
Ba	43.96	12.16
Totals	100.00	

Figure 7 XRD patterns of BaZryTi1−yO3; y = 0.0, 0.2 and 0.4 powders synthesized at 60 min sonication time (a) Enlarged ranges of 28-34o (b) Raman spectrum (c) and FT-IR spectrum (d) SEM/EDX results of the composition y = 0.4 powders (e and f).
101x76mm (300 x 300 DPI)

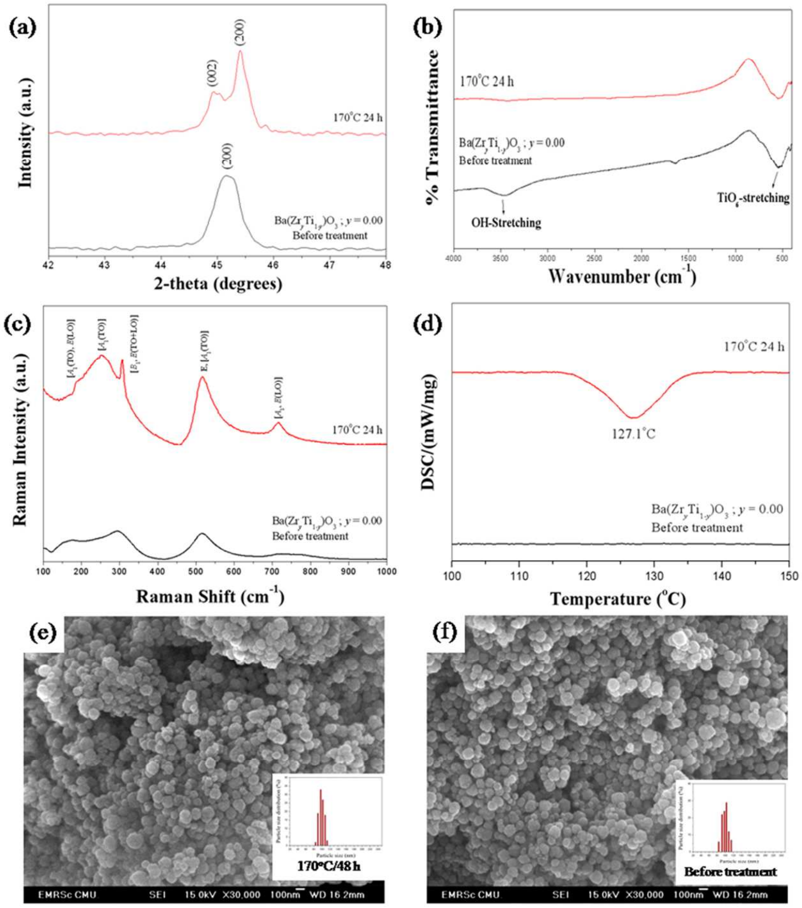

Figure 8 XRD pattern (a), FT-IR (b), Raman (c), DSC (d) and SEM image of BaZryTi1−yO3; y = 0.0 untreated powders (e) and chemically treated powders with DMF (f).
101x101mm (300 x 300 DPI)

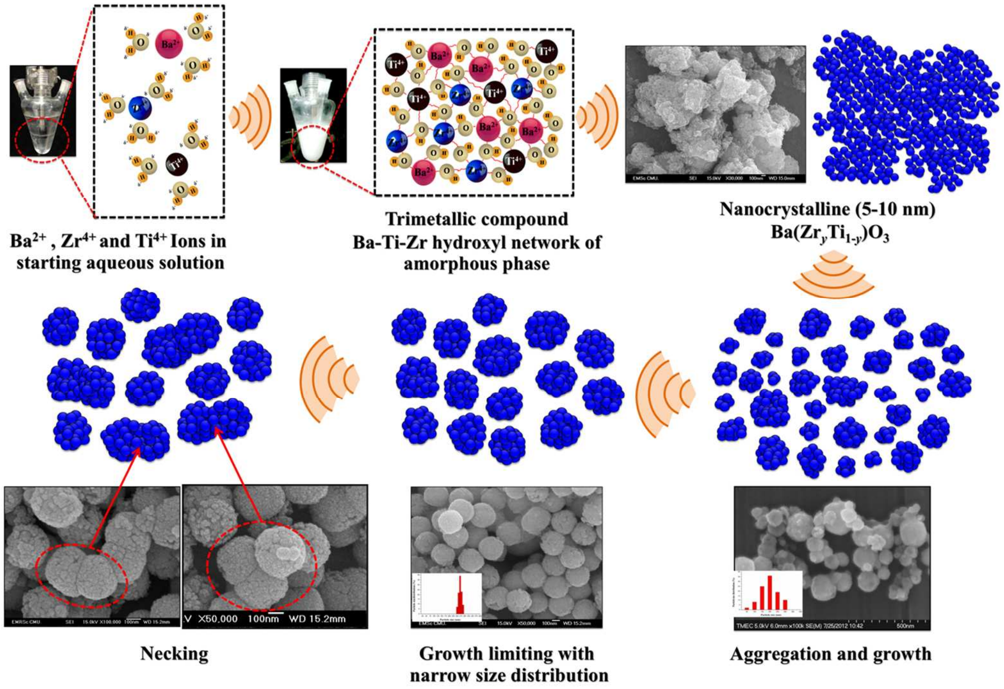

Figure 9 Schematic diagrams illustrating formation of the crystal growth mechanism.
127x88mm (300 x 300 DPI)